Computational Modelling of Concrete and Concrete Structures – Meschke, Pichler & Rots (Eds)
© 2022 Copyright the Author(s), ISBN: 978-1-032-32724-2

Numerical modelling via a coupled discrete approach of the autogenous healing for Fibre-Reinforced Cementitious Composites (FRCCs)

A. Cibelli, G. Di Luzio & L. Ferrara
Department of Civil and Environmental Engineering, Politecnico di Milano, Milan, Italy

ABSTRACT: Aiming to predict long-term performance of advanced cement-based materials and design more durable structures, a reliable modelling of the autogenous healing of cementitious materials is crucial. A discrete model for the regain in terms of water tightness, stiffness and strength induced by the autogenous and/or "žstimulate'ž autogenous healing was recently proposed for ordinary plain concrete. The modelling proposal stemmed from the coupling of two models, namely the Hygro-Thermo-Chemical (HTC) model, on one side, and the Lattice Discrete Particle Model (LDPM), on the other side, resulting in the Multiphysics-Lattice Discrete Particle Model (M-LDPM). Being this approach not customised only for ordinary concrete, but for the whole broad category of cementitious materials, in this paper, its application to Fibre-Reinforced Cementitious Composites is presented. To accurately simulate what has been experimentally observed so far, the mechanical model is updated to also include the self-healing of the *tunnel cracks* at the fibre-matrix interfaces. Therefore, the self-repairing process is modelled to develop on two independent stages: (a) matrix cracks healing, and (b) fibre bridging action restoring. This research activity is part of the modelling tasks framed into the project ReSHEALience, funded from the European Union's Horizon 2020 Research and Innovation Programme.

1 INTRODUCTION

The unavoidable concrete cracking and the ensuing degradation phenomena have encouraged many researchers to increase the efforts in enhancing the comprehension of such processes and the capability of modelling the concrete long-term performance. In this framework, the inherent healing capacity of cement based materials has been gaining an increasing interest by the concrete professional and scientific community. As demonstrated by several authors since its discovery (Snoeck & De Belie 2015), and mainly in the last decades, the self-healing of concrete can lead to a considerable recovery of physical and, in some cases, mechanical properties of damaged concrete.

Through a painstaking literature survey, an unbalanced scientific production clearly stands out. Over the years, an extensive research effort has been placed on the experimental investigation of the self-healing phenomenon, aiming to detect its peculiar features and which techniques were worth being further explored to turn it into a predictable and/or engineered process. On the contrary, few models have been developed to account for the healing-induced effects on both durability performance and mechanical behaviour. As a consequence, in literature there is a limited number of numerical studies on this phenomenon (Aliko-Benítez et al. 2015; Barbero et al. 2005; Chen et al. 2021; Davies & Jefferson 2017; Di Luzio et al. 2018; Hilloulin et al. 2014; Hilloulin et al. 2016; Mergheim & Steinmann 2013; Oucif et al. 2018; Voyiadjis et al. 2011). The majority of them relies on continuum-based approaches, leading to consider the aforementioned effects on the mechanical properties only as a smeared contribution in terms of either stiffness and/or strength regain in the cracked state. Likewise, the impact of the crack self-repairing on durability performance indicators, e.g. permeability, can be simulated only as an overall effect, missing in simulating the local nature of the phenomena, e.g. where the water permeability increases dramatically and restores after healing.

The research activity presented in this paper aims to formulate a discrete model for capturing the mechanical recovery induced by an actual damage healing into which the cracks sealing might eventually evolve.

Building more durable structures in order for concrete to result in a more sustainable material, developing sound models to predict the structural life span of concrete structures, and accounting for durability as a *governing* performance within the design process: these are only three of the many concurrent causes that have made the concrete durability worthwhile deserving an increasing interest by the scientific community. These issues also represent the guidelines of the Horizon 2020 project *ReSHEALience*, in which this work is framed. The project aims to define the concepts of Ultra High Durability Concrete (UHDC) and Durability Assessment-based Design (DAD). The UHDC material concept encompasses advanced cementitious

DOI 10.1201/9781003316404-10

materials which fully exploit their own inherent capacity of autonomously repairing the cracks. To the purpose, supplementary cementitious materials, such as slag and crystalline admixtures, are included into the mixture. In the project *ReSHEALience*, the identification of a quantitative approach to predict long-term performance of concrete structures, even when exposed to extremely aggressive environments, was performed through both laboratory experimental tests and monitoring campaigns on pilot UHDC structures exposed to real exposure conditions, together with the development of numerical models at meso- and macro-scale (Al-Obaidi et al. 2020, 2021; Lo Monte & Ferrara 2020, 2021).

2 RESEARCH BACKGROUND

The modelling proposal stems from the coupling of two models, namely the Hygro-Thermo-Chemical (HTC) model, on one side, and the Lattice Discrete Particle Model (LDPM), on the other side (Di Luzio & Cusatis 2009a, 2009b; Cusatis et al. 2011a, 2011b; Pathirage et al. 2019). The result is the Multiphysics-Lattice Discrete Particle Model (M-LDPM) (Abdellatef et al. 2015; Alnaggar et al. 2017; Cibelli et al. 2022; Yang et al. 2021).

2.1 Lattice Discrete Particle Model

In LDPM the geometrical configuration is generated by a trial-and-error random procedure, in which the aggregate particles, whose size distribution derives from a Fuller-type curve, are assumed to have spherical shape and are randomly placed within the volume. Then, zero-radius particles are located along the external surfaces to facilitate the imposition of boundary conditions. Based on the Delaunay tetrahedralisation of the generated system of points, a three-dimensional domain tessellation is carried out, and linear segments, namely tetrahedra edges, are generated to connect all particles centres. The outcome is a system of lattice-connected cells interacting through triangular facets: the mechanical interaction among particles is based on four particle-subsystems (Figure 1a), in which the spheres (nodes) are connected by struts (edges), having cross section (triangular facets) resulting from the volume tessellation (Figure 1b).

In LPDM, rigid body kinematics is employed to describe the deformation of the lattice particle system, and the displacement step $[\![\mathbf{u}_C]\!]$ at the centroid of each facet, C_k (Figure 1b), is used to define the strain measures which read $\varepsilon_N = (n^T[\![\mathbf{u}_C]\!])/l$; $\varepsilon_L = (l^T[\![\mathbf{u}_C]\!])/l$; $\varepsilon_M = (m^T[\![\mathbf{u}_C]\!])/l$, where n, l, m are the unit vectors which identify a local reference system on each facet in normal and shear directions, respectively.

Vectorial constitutive laws are defined at the centroid of each projected facet to describe the mesoscopic stress. In the elastic regime, normal and shear stresses are proportional to the corresponding strains: $\sigma_N = E_N\varepsilon_N$; $\sigma_L = E_T\varepsilon_L$; $\sigma_M = E_T\varepsilon_M$, where the elastic moduli are $E_N = E_0$ and $E_T = \alpha E_0$, in which E_0 is the effective normal modulus and α the shear-normal coupling parameter. One of the unique feature of the LDPM formulation consists of being able to automatically capture the effects of the heterogeneity of the concrete, such as splitting cracks and failure in compression, which can not be achieved by employing the classical theory of elasticity, e.g. see (Cusatis et al. 2011).

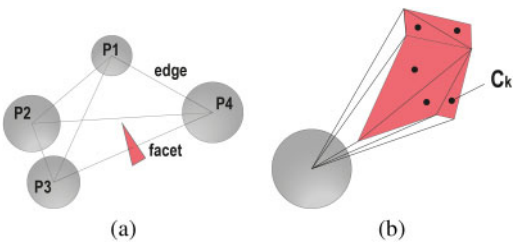

Figure 1. (a) four-particle subsystem; (b) triangular facets.

When in a facet under tension the strain reaches the tensile elastic limit, the meso-scale crack opening is calculated as $w_N = l(\varepsilon_N - \sigma_N/E_N)$; $w_L = l(\varepsilon_L - \sigma_L/E_T)$; $w_M = l(\varepsilon_M - \sigma_M/E_T)$. Then, the crack opening vector associated to each facet is $w_c = w_N n + w_L l + w_M m$, where w_N is the actual opening/closure of the crack, along the direction orthogonal to the facet, while w_L and w_M are two sliding components, catching shear displacements at crack surfaces.

The non-linear behaviour is analysed considering three non-linear meso-scale phenomena: (1) fracture and cohesion, (2) compaction and pore collapse, and (3) friction. For the latter two and further details about the model calibration and validation, the reader can refer to (Cusatis et al. 2011a, 2011b). Hereinafter, for the sake of clarity, the constitutive law for the fracturing behaviour is briefly recalled as the healing effect is therein implemented.

In LDPM the fracture behaviour is modelled by setting damage-type constitutive laws, which stem from the definition of effective strain, $\varepsilon = \sqrt{\varepsilon_N^2 + \alpha\left(\varepsilon_L^2 + \varepsilon_M^2\right)}$, and stress, $\sigma = \sqrt{\sigma_N^2 + \left(\sigma_L^2 + \sigma_M^2\right)/\alpha}$. Then, for tensile loading ($\varepsilon > 0$), the effective mechanical parameters permit to define the following relationships between strain and stress in the local reference systems: $\sigma_N = \varepsilon_N\,(\sigma/\varepsilon)$; $\sigma_L = \alpha\,\varepsilon_L\,(\sigma/\varepsilon)$; $\sigma_M = \alpha\,\varepsilon_M\,(\sigma/\varepsilon)$. The effective stress σ is incrementally elastic ($\dot{\sigma} = E_0\,\dot{\varepsilon}$) and must satisfy the inequality $0 \le \sigma \le \sigma_{bt}(\varepsilon,\,\omega)$, in which $\sigma_{bt}(\varepsilon,\omega)$ is a yield surface enforced by means of a vertical (at constant strain) return algorithm. The strain-dependent limit can be expressed as

$$\sigma_{bt}(\varepsilon,\omega) = \sigma_0(\omega)\exp\left[-H_0\,(\omega)\frac{\langle\varepsilon_{max} - \varepsilon_0\rangle}{\sigma_0(\omega)}\right] \qquad (1)$$

where the brackets $\langle\cdot\rangle$ are used in Macaulay sense: $\langle x\rangle = \max\{x, 0\}$, and H_0 is the post-peak softening

modulus, whose formulation allows for a smooth transition from a softening behaviour under pure tensile stress ($H_0(\omega=\pi/2)=H_t$) to perfectly plastic response under pure shear ($H_0(0)=0$). In fact, the formulation of H_0 reads $H_0(\omega)=H_t(2\omega/\pi)^{n_t}$, with n_t softening exponent.

In Eq. 1, ω is the parameter representing the degree of interaction between shear and normal loading. It is worth noting that ε_{max} is a history-dependent variable, making, on turn, the yield surface a history-dependent exponential function. Therefore, the actual fracture strength is assumed dependent on the actual level of damage. Finally, in Eq. 1 the function $\sigma_0(\omega)$ is the strength limit for the effective stress and is formulated as

$$\sigma_0(\omega)=\sigma_t\frac{-\sin(\omega)+\sqrt{\sin^2(\omega)+4\alpha\cos^2(\omega)/r_{st}^2}}{2\alpha\cos^2(\omega)/r_{st}^2} \quad (2)$$

in which $r_{st}=\sigma_s/\sigma_t$ is the ratio between the shear strength, σ_s (cohesion), and the tensile strength, σ_t.

2.2 Lattice Discrete Particle Model for FRC (LDPM-F)

The extension of LDPM to include fibre-reinforcing mechanisms is obtained by inserting straight fibers, in proportion to the volume fraction V_f, with random positions and orientations, into the LDPM geometrical configuration. The geometry of each individual fiber is characterised by the diameter d_f and length L_f. The fibre system is overlapped to the polyhedral cell system, and each facet is paired with its intersecting fibres. At the facet level, the matrix-fibre interaction is described by the bridging forces carried by the fibres crossing the facet, which are activated when the crack opening initiates. In this configuration, equilibrium considerations permit to reasonably assume a parallel coupling between the fibres and the surrounding concrete matrix. Then, the total stresses on each LDPM facet can be computed as $\sigma=\sigma_c+(\sum_{f\in A_c}P_f)/A_c$, where A_c is the facet area, and P_f represents the crack-bridging force for each fibre crossing the given facet.

Since the mechanical interaction between the fibres and the surrounding matrix occurs at a scale smaller than the typical modelling scale of LDPM, the micromechanics governing such interaction is not explicitly simulated in the mesoscopic LDPM numerical framework. The micro-mechanical crack-bridging mechanisms, featuring the bond between the single fibre and the embedding matrix, are implemented into the model within the formulation for computing the bridging force P_f, briefly reported hereinafter as it was published by (Schauffert & Cusatis 2012).

In addition to the above consideration, additional hypothesis are postulated: (i) the contribution of fibres to the equilibrium is negligible in case of either compression stress on the facet or stress not exceeding the elastic limit; (ii) the interaction between adjacent fibres and the effect that adjacent mesoscale cracks are both neglected; (iii) each fibre is assumed to be straight, elastic, with negligible bending stiffness, and non-circular cross sections are simulated through an equivalent diameter, calculated as $d_f=2(A_f/\pi)^{1/2}$ with A_f fibre cross-sectional area.

As proposed by Li et al. (Lin et al. 1999), in LDPM-F the slippage at full debonding v_d is computed as $v_d=(2\tau_0L_e^2)/(E_fd_f)+[(8G_dL_e^2)/(E_fd_f]^{1/2}$, in which L_e is the embedment length, E_f the modulus of elasticity of the fibre, τ_0 the constant value of frictional stress for the portion of the embedded fibre that has debonded, and G_d the bond fracture energy. The parameters τ_0 and G_d govern the debonding stage, modelled as a tunnel-type cracking process (Yang et al. 2008).

During the debonding stage ($v<v_d$), the fibre bridging force is given as (Lin et al. 1999)

$$P(v)=\left[\frac{\pi^2E_fd_f^3}{2}(\tau_0v+G_d)\right]^{1/2} \quad (3)$$

After full debonding ($v>v_d$), the mechanism is entirely frictional and the fibre load results from (Lin et al. 1999)

$$P(v)=P_0\left(1-\frac{v-v_d}{L_e}\right)\left[1+\frac{\beta\,(v-v_d)}{d_f}\right] \quad (4)$$

where $P_0=\pi L_ed_f\tau_0$, whereas β is the coefficient in charge of shaping the relationship to capture the high variability of the frictional interface nature (Lin & Li 1997). When the friction at the interface does not depend on the slippage, β is set to zero. In case of either slip hardening or slip softening friction, it assumes positive ($\beta>0$) or negative ($\beta<0$) values, respectively.

If the orientations of the embedded and free fibre portions is different, at the point where the fibre exits the matrix and changes orientation, the bearing stress is partially supported by the underlying matrix. When this localised stress field reaches a sufficient intensity, spalling occurs, and the embedment length of the fibre is consequently reduced by a length s_f. Furthermore, when the fibre exits the tunnel crack, the latter shortened because of the spalling, it wraps around the intact matrix. This phenomenon is generally referred to as *snubbing effect*, and it is modelled through the frictional pulley idealisation (Li et al. 1990), which complies with the fibre pull-out model adopted in the LDPM-F model (Yang et al. 2008). The fibre load is updated to account for spalling and snubbing phenomena (see (Schauffert & Cusatis 2012)). The updated value of the fibre load must comply with its rupture strength, then the following relationship must always hold: $\sigma_f=(4P_f)/(\pi d_f^2)\le\sigma_{u,f}\exp\left(-k_{rup}\varphi_f'\right)$, in which k_{rup} is a material parameter, and $\sigma_{u,f}$ the ultimate tensile strength of the fibre. In case of fibre stress exceeding the corrected value of strength, P_f is set to zero. The exponentional term reflects experimental evidence showing lower rupture loads in single fibre

pull-out tests for increasing values of φ_f' (Kanda & Li 1998).

For a generic fibre, with embedment segment orientation n_f, subject to pull-out from both embedment depths due to a crack opening w, and with a spalling length s_f on both sides, the crack-bridging force is given by $P_f = P_f \boldsymbol{n}_f'$, with the crack-bridging segment computed as $||\boldsymbol{w}'|| = 2s_f + v_s + v_l$ and $||\boldsymbol{n}'|| = \boldsymbol{w}'/||\boldsymbol{w}'||$, where $||\boldsymbol{w}'||$ is the vector length, and s_f the slippage reduction due to the matrix spalling. The embedment segments have the relative slippage v_s and v_l, respectively. The pullout resisting forces is then $P_f = P(v_s)\exp\left(k_{sn}\varphi_f'\right) = P(v_l)\exp\left(k_{sn}\varphi_f'\right)$, and on each side must be the same. From the last equality, the relative slippages v_s and v_l can be computed by an interactive procedure in which the compatibility between the bridging segment and the slippages is enforced.

Further details on the constitutive relations of fibres and matrix-fibre interaction as well as on the calibration of the governing parameters can be found in (Schauffert & Cusatis 2012; Schauffert et al. 2012).

3 MESOSCALE HEALING MODEL

The modelling approach relies on the identification of two different levels of damage: (i) matrix and (ii) fibre-matrix interface cracks. The matrix cracks (Figure 2a) are induced by the loads, either mechanical or environmental, and are responsible of the fibres mechanical activation: as long as no cracks intersect a fibre, the latter does not play any role in the structural response. The fibre-matrix interface cracks (Figure 2b) develop during the interface debonding instead, and are hereinafter also referred to as tunnel cracks between the fibre and the surrounding embedding matrix.

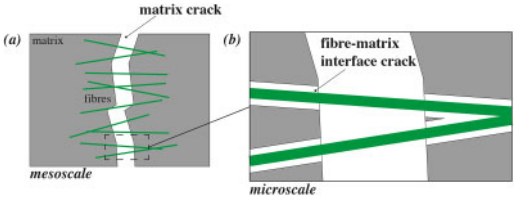

Figure 2. Two levels in the damage modelling: (a) **matrix cracks** at the mesoscale; (b) **fibre-matrix interface cracks** at the microscale.

The self-healing model is in line with the LDPM approach, dealing with matrix and tunnel cracks separately. The autogenous repairing of the former is implemented within the constitutive fracture law at the mesoscale, whereas the effect of healing on the fibres response is taken into account within the calculation of the bridging force carried by the steel reinforcement. This approach stems from the idea for which the recovery of matrix damage and tunnel cracks along fibre-mortar interface affect the material mechanical behaviour differently.

3.1 *Healing characterization*

The healing kinetic law formulated for plain cementitious materials (Di Luzio et al. 2018; Cibelli et al. 2022) presents no limitations in being used for fibre-reinforced composites as well. Following the conceptual differentiation between matrix and tunnel cracks, it can be exploited for capturing the autogenous, and eventually stimulated, healing of the matrix cracks. On the other hand, in order to have two separate internal variables feeding the mechanical model at two different levels, in the improved version of M-LDPM a distinction is made between the normalised healing degree for matrix cracks and that for fibre-matrix interface cracks, λ_{sh}^m and λ_{sh}^f respectively. In the following the formulation emphasising such splitting is reported, with no theoretical differences with respect to the original one (Di Luzio et al. 2018).

The kinetic laws for matrix (superscript m) and tunnel (superscript f) cracks read

$$\dot{\lambda}_{sh}^m = \tilde{A}_{sh}^m\left(1 - \lambda_{sh}^m\right) \tag{5a}$$

$$\dot{\lambda}_{sh}^f = \tilde{A}_{sh}^f\left(1 - \lambda_{sh}^f\right) \tag{5b}$$

in which $\tilde{A}_{sh}^m$ and $\tilde{A}_{sh}^f$, inversely proportional to the reaction characteristic times, are calculated as

$$\tilde{A}_{sh}^m = \tilde{A}_{sh0}^m \cdot f_h(h) \cdot f_w^m(w_c) \cdot e^{\left[-E_{sh}^m/R\left(1/T - 1/T_{ref}\right)\right]} \tag{6a}$$

$$\tilde{A}_{sh}^f = \tilde{A}_{sh0}^f \cdot f_h(h) \cdot f_w^f(w_c) \cdot e^{\left[-E_{sh}^f/R\left(1/T - 1/T_{ref}\right)\right]} \tag{6b}$$

where $\tilde{A}_{sh.0}^m$ and $\tilde{A}_{sh.0}^f$, namely the inverse of the reaction characteristic times in standard conditions (RH=100%, $T = T_{ref}$, $w_c = 0$), value

$$\tilde{A}_{sh0}^m = \tilde{A}_{sh1}^m\left(1 - \alpha_c^{sh0}\right)c + \tilde{A}_{sh2}^m \cdot ad \tag{7a}$$

$$\tilde{A}_{sh0}^f = \tilde{A}_{sh1}^f\left(1 - \alpha_c^{sh0}\right)c + \tilde{A}_{sh2}^f \cdot ad \tag{7b}$$

where c and ad are the cement and healing-promoting admixture content, respectively. The material parameters E_{sh}^m, E_{sh}^f, $\tilde{A}_{sh1}^m$, $\tilde{A}_{sh1}^f$, $\tilde{A}_{sh2}^m$, and $\tilde{A}_{sh2}^f$ are calibrated against experimental data, allowing to catch the peculiarities of phenomena occurring at two different scales. Furthermore, the double degree of freedom permits to properly simulate the effect of crack opening, modelled through the coefficient $f_w(w_c)$, on the process evolution. The coefficient $f_h(h)$ accounts for relative humidity and simulates the relevant role played by the moisture supply, making the process proceed or stop whether the healing water-driven reactions are fed or not. In the Eqs. the relative humidity, h, and temperature, T, fields are provided by the HTC model.

3.2 *Healing implementation in LDPM and LDPM-F*

The healing-induced effect on the mechanical response of the cementitious materials involves recovery of post-cracking residual fracture strength. Depending on

which cracks are healed, the aforementioned recovery is the result of different physical phenomena. For this reason, the implementation in the mechanical models follows two separate dedicated approaches.

3.2.1 *Matrix cracks*

For matrix cracks, the healing effect is modelled by enforcing a homothetic expansion of the boundary limit curve $\sigma_{bt}(\varepsilon, \omega)$ (Eq. 1), as more pronounced as more the repairing process has developed.

What has been experimentally observed so far is that plain concrete specimens, once loaded, fractured and unloaded, might show a recovery in strength and stiffness if re-loaded after a long enough curing period. It is due to the concurring delayed hydration and carbonation self-healing mechanisms. This partially restores the material continuity, having straightforward consequences on the concrete bulk permeability and its proneness to the attacks of environmental aggressive agents. The effects on the mechanical response, instead, depend on the chemical bounds between the filling products and the crack walls; then, it is not granted that the recovery in water tightness and the regain in strength and stiffness proceed to the same extent. In fact, the crack sealing might not result in an actual concrete healing.

With reference to plain concrete specimens, precracked by means of three-point bending tests up to damage threshold beyond the material linear limit (Eq. 2), the healing effect on fracture behaviour might be measured by carrying out the same fracture tests after varying curing periods. The recorded load-CMOD curve may show reloading branches (1) stiffer than the unloading ones, and (2) crossing the un-healed material boundary curve (Figure 3).

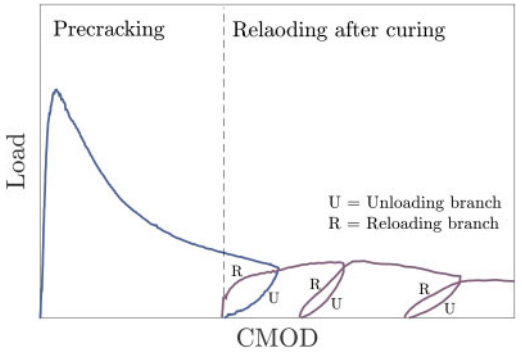

Figure 3. An example of the experimental curves gained in a laboratory campaign to assess the mechanical regain induced by the autogenous healing (Ferrara et al. 2014).

In this work, the modelling strategy adopted aims at preserving the inherent mechanical meaning of the impact due to the healing on the fracture strength, and relies on the homothetic expansion of the boundary curve (Figure 4). The expansion extent is assumed to be proportional to the healing degree λ_{sh}^m, thus capturing the recovery in strength, without varying the

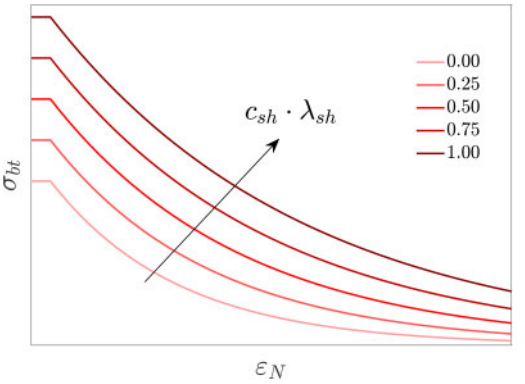

Figure 4. **matrix cracks -** Effect of healing on the boundary curve for the fracturing behaviour.

crack width within the numerical framework. In other words, the boundary expansion is conceived to catch the behaviour described above: the material must be allowed to overcome the strength value reached at the beginning of the unloading branch, for the previously reached value of crack width, if any healing has occurred.

In LDPM, the healing implementation affects the strength limit calculation (Eq. 2), thus, on turn, the limit curve (Eq. 1). The updated version of the healing dependent-constitutive law relevant to the fracture behaviour reads

$$\sigma_0(\omega, \lambda_{sh}^m) = \sigma_0(\omega)\ \left(1 + c_{sh} \cdot \lambda_{sh}^m\right) \tag{8a}$$

$$\sigma_{bt}(\varepsilon, \omega, \lambda_{sh}^m) = \sigma_0(\omega, \lambda_{sh}^m)\, e^{\left[-H_0(\omega)\frac{\langle \varepsilon_{max} - \varepsilon_0 \rangle}{\sigma_0(\omega, \lambda_{sh}^m)}\right]} \tag{8b}$$

In Eq. 8a, c_{sh} is an empirical coefficient governing the impact of crack closure on mechanical strength. It is defined as *healing mechanical impact coefficient*. The parameter c_{sh} depends on several aspects, e.g. curing conditions and mixture composition, therefore, it has to be calibrated experimentally.

Looking at the updated equation of the boundary curve (Eq. 8b), it is important to notice that the healing *plays* an active role as internal variable in both shaping the softening branch and setting the stress limit for the earlier stage of the constitutive law, namely when the maximum strain does not exceed the elastic limit. It is worth emphasising that, though the modelling strategy yields a recovery of both linear and post-peak behavior,the former is never imposed at the mesoscale, being only the limit curve expanded exclusively on those facets which experience cracking and healing.

3.2.2 *Fibre-matrix interface cracks*

With single-fibre pull-out tests, stopped after the first load drop and resumed up to rupture after curing periods featuring different duration and exposure conditions, it has been observed that the healing of the interface cracks does affect the pull-out strength.

Whenever the healing process happens, it yields delayed hydration products and $CaCO_3$ crystals fulfilling the tunnel between the fibre and the surrounding mortar ((Qiu et al. 2019)). This results in a recovery of the interface frictional bond. The phenomenon is implemented in LDPM-F by updating the value of the fibre bridging force $P(v)$ with a coefficient proportional to λ_{sh}^{f}. The updated constitutive law for the fibre load reads

$$P\left(v, \lambda_{sh}^{f}\right) = \left(1 + \gamma_{sh} \cdot \lambda_{sh}^{f}\right) P(v) \leq \alpha \cdot P_0 \tag{9}$$

Referring to a single-fibre pull-out test, in Figure 5 the effect of the tunnel crack self-healing on the mechanical response is qualitatively shown. After the loading and unloading stages (branches L and U), the specimen is exposed to given environmental conditions for a time span long enough to permit the self-healing process to develop. The cured specimen is then reloaded (branch R) up to rupture. Due to the recovered frictional bond, the specimen might experience a recovery in stiffness and strength, to an extent proportional to the degree of completion of the healing process. By means of the device in Eq. 9 LDPM-F is updated to be capable of capturing this experimental evidence. In Figure 5 the updated constitutive law is plotted with reference to increasing self-healing degrees, in the hypothesis of $\gamma_{sh} = 1.00$.

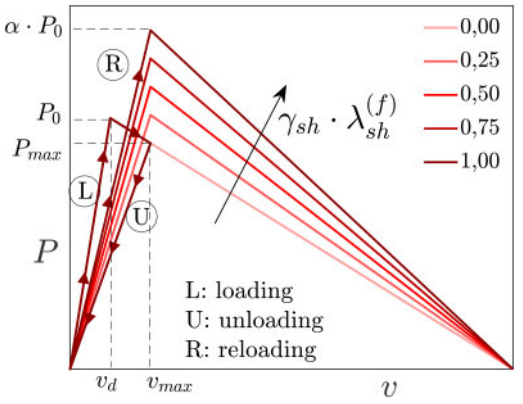

Figure 5. **fibre-matrix interface cracks -** Effect of healing on the fibre load vs. slippage law.

The coefficient γ_{sh} has a physical meaning similar to c_{sh}. It governs the impact that the healing of the tunnel cracks has on the fibres contribution to the mechanical equilibrium. With $\gamma_{sh} = 0$ it is possible to capture the crack sealing, whereas if $\gamma_{sh} \geq 0$ the load carried by the fibre is enhanced thanks to the increased friction along the crack walls. The latter has an upper bound ($\alpha \cdot P_0$) in which the bridging force at full debonding P_0 is either amplified or reduced by the coefficient α. Both γ_{sh} and α are material parameters to calibrate against experimental data. Depending on the composition of the cementitious composites, the technique adopted to engineer the process, the fibres nature, the curing conditions, and the loading regimes the healing might allow to recover either partially or entirely the fibre load bearing capacity. The parameter α sets the maximum achievable level of recovery. Once calibrated experimentally, γ_{sh} must comply with the condition for which, in case of full fulfilment of the tunnel crack:

$$\text{if} \quad \lambda_{sh}^{f} = 1.00 \Longrightarrow \gamma_{sh} \leq \frac{\alpha \cdot P_0}{P(v)} - 1 \tag{10}$$

4 NUMERICAL SIMULATIONS

4.1 Healing of matrix cracks

The concrete self-healing is expected to affect the meso-scale mechanical response of the material, in tension as much as in shear. The model has been implemented to catch this phenomenon, with the possibility of calibrating the entity of the induced strength recovery by means of the parameter c_{sh}. In order to investigate the model capability of capturing the self-repairing effect on tensile and shear behaviours, the numerical simulations of how two ordinary plain concrete (OPC) specimens behave after being damaged in tension and brought to collapse, after curing, either in pure tension or shear have been executed.

Table 1. Mix composition of the reference concrete (dosages in kg/m^3).

constituent	content
cement	300
water	190
aggregates 5.5-16 mm	1950

The material adopted has been an ordinary plain concrete whose mix composition is presented in Table 1.

Concerning the geometry, the collapse in tension has been investigated for a dogbone specimen, as usual for pure tensile tests, having the dimensions reported in Figure 6a and thickness of 20 mm. These dimensions have been chosen in order to have the narrowest part of the sample larger than the maximum aggregate size of the adopted material, and, at the same time, as smaller as possible to localise there the damage. The other geometrical characteristics have been set accordingly, with the aim of having a sample weak at the midspan, and the parts 70 mm wide covering a portion of the total length as smaller as possible. For the shear failure, instead, a bi-notched prismatic specimen has been used (Figure 6b), having dimensions 100x70x20 mm^3, and the notches 2 mm wide and 25 mm deep. In this case, it has been necessary to avoid a slender sample, as the dog-bone specimen presented above is. In fact, a stocky element presents a larger proneness

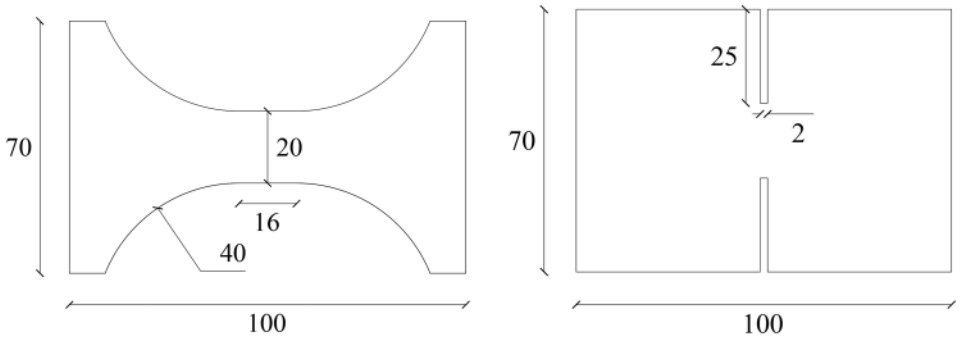

(a) Dogbone specimen: dimensions. (b) Notched specimen: dimensions.

Figure 6. Geometrical dimensions of the simulated specimens in millimetres.

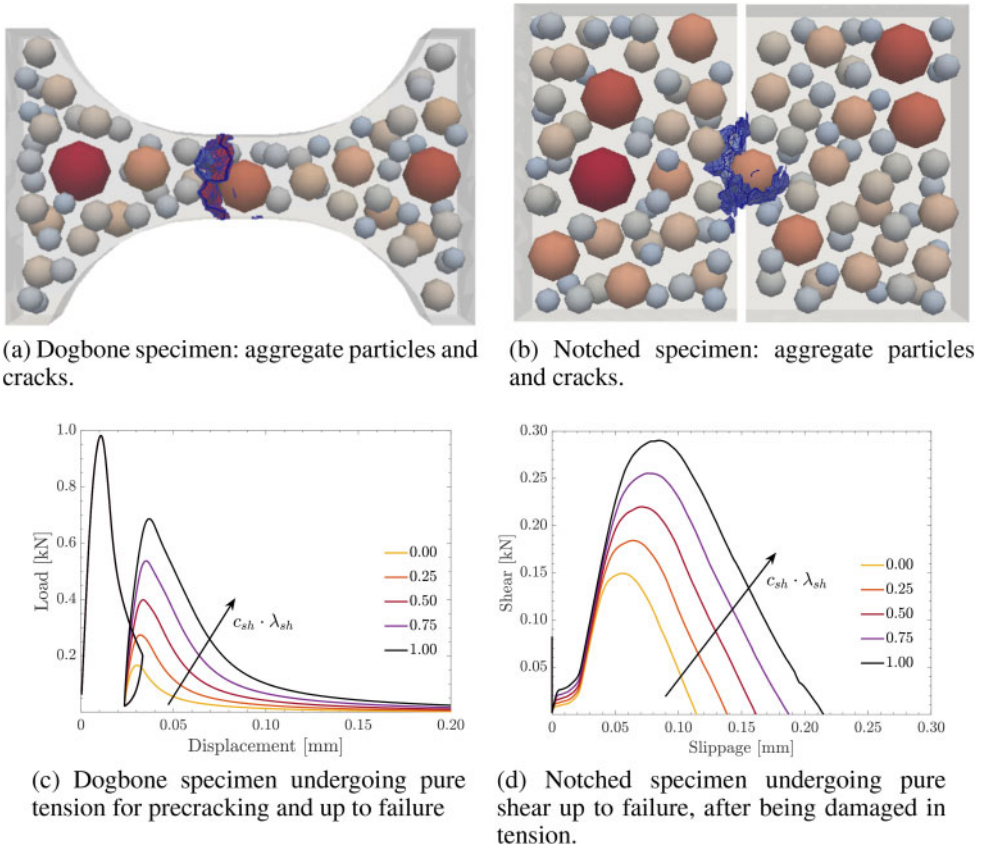

(a) Dogbone specimen: aggregate particles and cracks.

(b) Notched specimen: aggregate particles and cracks.

(c) Dogbone specimen undergoing pure tension for precracking and up to failure

(d) Notched specimen undergoing pure shear up to failure, after being damaged in tension.

Figure 7. LDPM modelled specimens for assessing the influence of healing implementation on (a) tension and (b) shear behaviours.

to shear failure. However, likewise for the investigation in pure tension, it has been necessary to shape the sample in order to have all the mechanical energy channelled into the growth of the fracture at the mid-span, with no dispersion due to multi-cracking scenarios. For this reason, it has been used a bi-notched shape, with narrow and deep notches. It is worth mentioning that also in this case the narrowest sample cross-section has been set in order to have the smallest dimension larger than the maximum aggregate size. The other dimensions have been derived to result in a stocky sample.

Once the samples geometry has been generated, both specimens have been damaged by means of

an increasing tensile loading, up showing a single crack roughly 350μm wide (Figures 7a,b). Afterwards, the dog-bone sample has been brought to failure in tension, whereas the bi-notched one in shear. This second stage has been repeated after having imposed increasing value of the normalised healing degree, λ_{sh}^{m}, ranging from 0.00 to 1.00, and in the hypothesis of having unit healing mechanical impact coefficient, c_{sh}. Then, in Figures 7c,d, the model ability of catching the healing-induced recovery in tensile and shear strength is shown plotting the (e) tensile load vs. displacement and (f) shear load vs. slippage curves.

4.2 Healing of tunnel cracks

The dogbone specimen in Figure 6a has been used also for testing the implementation of the tunnel cracks healing, by generating a FRC-based mesh with the same geometry. The concrete composition is reported in Table 2, where it is possible to see that the aggregate size has been reduced in order to have fibres length complying with specimen dimensions and aggregate size: $L_f \geq 3D_{max}$.

Table 2. Mix composition of the reference fibre-reinforced concrete (dosages in kg/m^3).

constituent	content
cement	600
water	200
aggregates 3-6 mm	1518
steel fibres $d_f = 0.22$ mm, $L_f = 20$ mm	0.50% by volume

As for matrix cracks, the purpose of investigating if the healing implementation affects the fibre load-slippage constitutive law as shown in Figure 5 is achieved through a simple set of numerical simulations. The dogbone specimens has been loaded in pure axial tension up to feature a single prominent crack approximately 60μm wide. Then, it has been completely unloaded. After having reached the zero-load condition, the sample has been reloaded up to failure. The reloading stage has been performed by assuming for the tunnel cracks self-healing degree, λ_{sh}^{f}, increasing fixed values between 0.00 and 1.00, namely 0.00, 0.25, 0.50, 0.75, and 1.00. The numerical simulations have been carried out in two different scenarios: with no matrix cracks healing, $\lambda_{sh}^{m} = 0.00$, and in the hypothesis of matrix and tunnel cracks healing evolving identically, $\lambda_{sh}^{m} = \lambda_{sh}^{f}$.

Firstly, it is important to assess how the model performs at the single fibre-facet intersection, to see if the P-v curve actually evolves as presented in Figure 5. The comparison between the fibre load vs. slippage curves on one of the most damaged LDPM facets obtained with λ_{sh}^{f} equals to 0.00 and 1.00 are shown in Figure 8b. The effect of healing acts as expected, though the re-loading in presence of healing stops before reaching the ultimate slippage (Figure 8b). In fact, as stands out from Figures 8c,d, in the numerical simulations the specimen experiences a sudden drop in strength, disregarding whether the healing of the matrix cracks is considered or not.

5 CLOSING REMARKS

The healing implementation for both matrix and tunnel cracks show promising capability in capturing the experimental evidence.

The healing of the matrix cracks affects the macroscale response of the two specimens as expected, in tension as much as in shear. With an increasing healing degree, in the hypothesis of $c_{sh} = 1.00$, the material experiences increasing stiffness during the re-loading and higher strength. It is worth underlining that the full recovery occurs at the mesoscale, shaping the macroscale behaviour accordingly. The peak load after re-loading, even in case of $c_{sh} \cdot \lambda_{sh}^{m} = 1.00$ on the damaged facets, is not equals to the peak load of the virgin material. This is in line with laboratory results showing that the hydration outcomes at the crack faces, the main contributors to autogenous cracks healing, have generally lower performance compared to those in bulk cement paste.

With $\lambda_{sh}^{m} = 0.00$ and increasing λ_{sh}^{f} ($\gamma_{sh} = 1.00$), the model returns a recovery in stiffness and strength during the re-loading, even though the numerical results do not show a stable re-loading branch when the slippage overcomes the value of the pre-cracking stage. This is likely due to the limited energy redistribution allowed by the specimen geometry, imposed by the necessity of having localised damage. This deduction is justified also by the fibre load vs. slippage curve on the most damaged facets. It is evident that the specimen failure anticipates the full depletion of the load-bearing capacity of the system fibre-matrix.

In case of $\lambda_{sh}^{m} = \lambda_{sh}^{f}$ ($\gamma_{sh} = 1.00$), the recovery in stiffness and strength is more pronounced as expected. Also in this condition, the limited energy redistribution due to specimen geometry does not permit to exploit the full material ductility.

The model presented seems to have the potential for capturing phenomenological trends and mechanics standing out from the experimental investigations available in the literature. However, the calibration and validation against laboratory results, currently matter of study, will help in further improving the proposed approach.

ACKNOWLEDGMENTS

The work described in this paper has been performed in the framework of the project ReSHEALience - Rethinking coastal defence and green-energy Service

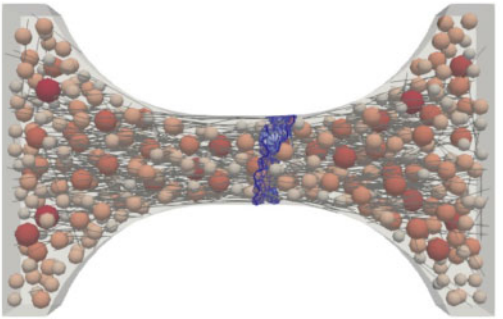

(a) Dogbone FRC specimen: aggregate particles, fibres and cracks.

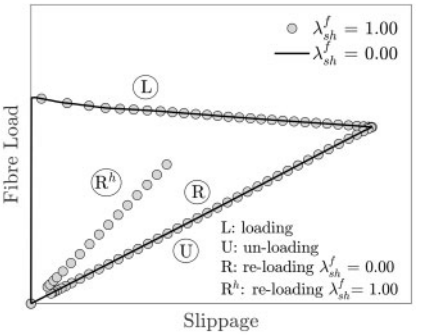

(b) Fibre load vs. slippage curve experienced along one of the most damaged facets.

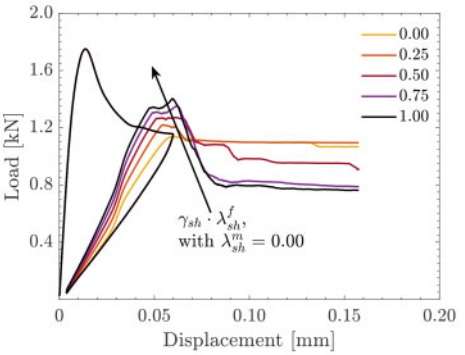

(c) Pure tension for precracking and up to failure with only tunnel cracks healing.

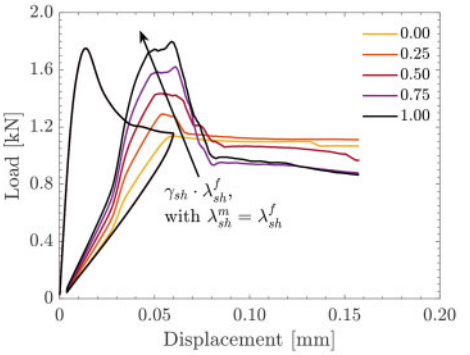

(d) Pure tension for precracking and up to failure with both matrix and tunnel cracks healing.

Figure 8. Influence of healing implementation on FRC dogbone specimen under uniaxial tension load.

infrastructures through enHancEd-durAbiLity high-performance cement-based materials, whose funding the first, fourth and last author gratefully acknowledge. This project has received funding from the European Union Horizon 2020 research and innovation programme under grant agreement No 760824. The information and views set out in this publication do not necessarily reflect the official opinion of the European Commission. Neither the European Union institutions and bodies nor any person acting on their behalf, may be held responsible for the use which may be made of the information contained therein. The numerical analyses have been performed by means of MARS, an explicit dynamic code distributed by ES3 Inc. (Engineering and Software System Solutions), which is gratefully acknowledged.

REFERENCES

Abdellatef, M., M. Alnaggar, G. Boumakis, G. Cusatis, G. Di Luzio, & R. Wendner (2015, September 21–23). Lattice discrete particle modeling for coupled concrete creep and shrinkage using the solidification microprestress theory. In C. Hellmich, B. Pichler, and J. Kollegger (Eds.), *10th International Conference on Mechanics and Physics of Creep, Shrinkage, and Durability of Concrete and Concrete Structures - CONCREEP-10*, Vienna, Austria, pp. 184–193.

Al-Obaidi, S., P. Bamonte, F. Animato, F. Lo Monte, I. Mazzantini, M. Luchini, S. Scalari, & L. Ferrara (2021). Innovative design concept of cooling water tanks/basins in geothermal power plants using ultra-high-performance fiber-reinforced concrete with enhanced durability. *Sustainability 13*(17).

Al-Obaidi, S., P. Bamonte, M. Luchini, I. Mazzantini, & L. Ferrara (2020). Durability-based design of structures made with ultra-high-performance/ultra-high-durability concrete in extremely aggressive scenarios: Application to a geothermal water basin case study. *Infrastructures 5*(11).

Aliko-Benítez, A., M. Doblaré, & J. Sanz-Herrera (2015). Chemical-diffusive modeling of the self-healing behavior in concrete. *International Journal of Solids and Structures 69-70*, 392–402.

Alnaggar, M., G. Di Luzio, & G. Cusatis (2017). Modeling time-dependent behavior of concrete affected by alkali silica reaction in variable environmental conditions. *Materials 10*(5).

Barbero, E. J., F. Greco, & P. Lonetti (2005). Continuum damage-healing mechanics with application to self-healing composites. *International Journal of Damage Mechanics 14*(1), 51–81.

Chen, Q., X. Liu, H. Zhu, J. W. Ju, X. Yongjian, Z. Jiang, & Z. Yan (2021). Continuum damage-healing framework for the hydration induced self-healing of the cementitious composite. *International Journal of Damage Mechanics 30*(5), 681–699.

Cibelli, A., M. Pathirage, L. Ferrara, G. Cusatis, & G. Di Luzio (2022). A discrete numerical model for the effects of crack healing on the behaviour of ordinary plain concrete: Implementation, calibration, and validation. *Engineering Fracture Mechanics in press*.

Cusatis, G., A. Mencarelli, D. Pelessone, & J. Baylot (2011). Lattice discrete particle model (LDPM) for failure behavior of concrete. II: Calibration and validation. *Cement and Concrete Composites 33*(9), 891–905.

Cusatis, G., D. Pelessone, & A. Mencarelli (2011). Lattice discrete particle model (LDPM) for failure behavior of concrete. I: Theory. *Cement and Concrete Composites 33*(9), 881–890.

Davies, R. & A. Jefferson (2017). Micromechanical modelling of self-healing cementitious materials. *International Journal of Solids and Structures 113-114*, 180–191.

Di Luzio, G. & G. Cusatis (2009a). Hygro-thermo-chemical modeling of high-performance concrete. II: Numerical implementation, calibration, and validation. *Cement and Concrete Composites 31*(5), 309–324.

Di Luzio, G. & G. Cusatis (2009b). Hygro-thermo-chemical modeling of high performance concrete. II: Theory. *Cement and Concrete Composites 31*(5), 301–308.

Di Luzio, G., L. Ferrara, & V. Krelani (2018). Numerical modeling of mechanical regain due to self-healing in cement based composites. *Cement and Concrete Composites 86*, 190–205.

Ferrara, L., V. Krelani, & M. Carsana (2014). A "fracture testing" based approach to assess crack healing of concrete with and without crystalline admixtures. *Construction and Building Materials 68*, 535–551.

Hilloulin, B., F. Grondin, M.Matallah, & A. Loukili (2014). Modelling of autogenous healing in ultra high performance concrete. *Cement and Concrete Research 61-62*, 64–70.

Hilloulin, B., D. Hilloulin, F. Grondin, A. Loukili, & N. De Belie (2016). Mechanical regains due to self-healing in cementitious materials: Experimental measurements and micro-mechanical model. *Cement and Concrete Research 80*, 21–32.

Kanda, T. & V. C. Li (1998). Interface property and apparent strength of high-strength hydrophilic fiber in cement matrix. *Journal of Materials in Civil Engineering 10*(1), 5–13.

Li, V., Y. Wang, & S. Backer (1990). Effect of inclining angle, bundling and surface treatment on synthetic fibre pull-out from a cement matrix. *Composites 21*(2), 132–140.

Lin, Z., T. Kanda, & V. C. Li (1999). On interface property characterization and performance of fiber reinforced cementitious composites. *Journal of Concrete Science and Engineering, RILEM 1*, 173–184.

Lin, Z. & V. C. Li (1997). Crack bridging in fiber reinforced cementitious composites with slip-hardening interfaces. *Journal of the Mechanics and Physics of Solids 45*(5), 763–787.

Lo Monte, F. & L. Ferrara (2020). Tensile behaviour identification in ultra-high performance fibre reinforced cementitious composites: indirect tension tests and back analysis of flexural test results. *Materials and Structures 53*(6), 145.

Lo Monte, F. & L. Ferrara (2021). Self-healing characterization of uhpfrcc with crystalline admixture: Experimental assessment via multi-test/multi-parameter approach. *Construction and Building Materials 283*, 122579.

Mergheim, J. & P. Steinmann (2013). Phenomenological modelling of self-healing polymers based on integrated healing agents. *Computational Mechanics 52*(3), 681–692.

Oucif, C., G. Z. Voyiadjis, & T. Rabczuk (2018). Modeling of damage-healing and nonlinear self-healing concrete behavior: Application to coupled and uncoupled self-healing mechanisms. *Theoretical and Applied Fracture Mechanics 96*, 216–230.

Pathirage, M., D. Bentz, G. Di Luzio, E. Masoero, & G. Cusatis (2019). The onix model: a parameter-free multiscale framework for the prediction of self-desiccation in concrete. *Cement and Concrete Composites 103*, 36–48.

Qiu, J., S. He, Q. Wang, H. Su, & E. Yang (2019). Autogenous healing of fiber/matrix interface and its enhancement. *Proc. of the 10st Intern. Conf. on Fracture Mechanics of Concrete and Concrete Structures (FraMCoS-X), G. Pijaudier-Cabot, P. Grassl and C. La Borderie Eds. 24-26 June, Bayonne, France*.

Schauffert, E. A. & G. Cusatis (2012). Lattice discrete particle model for fiber-reinforced concrete. i: Theory. *Journal of Engineering Mechanics 138*(7), 826–833.

Schauffert, E. A., G. Cusatis, D. Pelessone, J. L. O'Daniel, & J. T. Baylot (2012). Lattice discrete particle model for fiber-reinforced concrete. ii: Tensile fracture and multiaxial loading behavior. *Journal of Engineering Mechanics 138*(7), 834–841.

Snoeck, D. & N. De Belie (2015). From straw in bricks to modern use of microfibers in cementitious composites for improved autogenous healing – a review. *Construction and Building Materials 95*, 774–787.

Voyiadjis, G. Z., A. Shojaei, & G. Li (2011). A thermodynamic consistent damage and healing model for self healing materials. *International Journal of Plasticity 27*(7), 1025–1044.

Yang, E.-H., S. Wang, Y. Yang, & V. C. Li (2008). Fiber-bridging constitutive law of engineered cementitious composites. *Journal of Advanced Concrete Technology 6*(1), 181–193.

Yang, L., M. Pathirage, H. Su, M. Alnaggar, G. Di Luzio, & G. Cusatis (2021). Computational modeling of temperature and relative humidity effects on concrete expansion due to alkali–silica reaction. *Cement and Concrete Composites 124*, 104237.